Supporting Information

Efficient Hydrogen Evolution Catalyst Constructed by Pt-Modified Ni$_3$S$_2$/MoS$_2$ with Optimized Kinetics Across the Full pH Range

Maoyuan Li[a#], Zhongrui Yu[b#], Zulin Sun[a#], Yuchen Liu[c], Simiao Sha[a], Jiancheng Li[a], Riyue Ge[d], Liming Dai[e,f], Bin Liu[a,*], Qingqiao Fu [a,*], Wenxian Li[e,f,*]

[a] School of Materials Science and Engineering, Shanghai University, Shanghai 200444, China

[b] Shanghai Electric Hency Solar Technology Co., ltd, Shanghai Electric Power Generation Group, Shanghai, 201199, China

[c]School of Science, Nanjing Agricultural University, Nanjing 210095, China

[d] School of Fashion and Textiles, The Hong Kong Polytechnic University, Hung Hom, Kowloon 999077, Hong Kong

[e] School of Chemical Engineering, The University of New South Wales, Sydney, New South Wales 2052, Australia

[f] Australian Research Council Centre of Excellence for Carbon Science and Innovation, The University of New South Wales, Sydney, New South Wales 2052, Australia

*E-mail addresses: binliu@shu.edu.cn (Bin Liu), fuqingqiao@shu.edu.cn (Qingqiao Fu), wenxian.li1@unsw.edu.au (Wenxian Li)

[#]Authors contributed to this work equally.

1. Experimental

1.1 Materials synthesis

Nickel foam (3×2 cm²) was pretreated by ultrasonic cleaning in a 3 M hydrochloric acid solution for 15 minutes to remove surface oxides and impurities. Subsequently, the foam was thoroughly washed with deionized water and ethanol through ultrasonic cleaning to eliminate any residual contaminants and solvents. To grow Ni$_3$S$_2$/MoS$_2$ nanorod arrays on the nickel foam, a hydrothermal method was employed as follows: 60 mg of ammonium heptamolybdate tetrahydrate ((NH$_4$)$_6$Mo$_7$O$_{24}$·4H$_2$O), 110 mg of thiourea (C$_2$H$_5$NS), and 40 mg of sodium acetate (CH$_3$COONa) were dissolved in 30

mL of deionized water and stirred until completely dissolved. The resulting solution, along with the cleaned nickel foam, was then transferred into a 50 mL polytetrafluoroethylene-lined stainless-steel autoclave. The autoclave was placed in a forced air oven and heated to 180 °C at a rate of 5 °C min^{-1}, where it was maintained for 16 hours. After cooling to room temperature, the sample was washed several times with deionized water and anhydrous ethanol, and then dried overnight in a vacuum oven. The resulting sample was denoted as Ni_3S_2/MoS_2.

1.2 X-ray Diffraction (XRD) Analysis

The crystal structure of the materials was characterized using XRD with Cu-Kα radiation. The diffraction measurements were performed with a scan rate of 4°/min to assess the phase composition and crystallinity of the catalyst materials.

1.3 Scanning Electron Microscopy (SEM)

Surface morphology and elemental composition were analyzed using a ZEISS Gemini 300 SEM. The operating conditions included an acceleration voltage of 3 kV and a probe current ranging from 3 pA to 20 nA. Images were acquired at magnifications ranging from 500 to 80,000. Elemental information was obtained using backscattered electrons, which provided details on surface topography and elemental distribution.

1.4 X-ray Photoelectron Spectroscopy (XPS)

Surface chemical states and elemental compositions were investigated using XPS with a Thermo Scientific K-Alpha spectrometer. The measurements were conducted at a working voltage of 12 kV using Al Kα radiation (hv = 1486.6 eV) with a filament current of 6 mA. This technique enabled the analysis of surface chemical elements and their oxidation states.

1.5 Transmission Electron Microscopy (TEM/HAADF-STEM)

The thickness and density of the samples were determined using a JEOL JEM-F200

TEM equipped with HAADF-STEM detector. The acceleration voltage was set at 200 kV, and EDS was performed with a JED-2300T system. Electron diffraction patterns were collected to elucidate the crystal structure of the samples.

1.6 Brunauer-Emmett-Teller (BET) Surface Area Measurement

The specific surface area of the samples was calculated using the BET method, based on nitrogen adsorption data. The nitrogen adsorption isotherms were analyzed according to the equation:

$$\frac{P}{V(P_0 - P)} = \frac{1}{V_m \times C} + \frac{C - 1}{V_m \times C} \times \frac{P}{P_0} \tag{1}$$

where P is the nitrogen pressure, P_0 is the nitrogen saturation vapor pressure, V is the actual nitrogen adsorption amount on the sample surface, V_m is the monolayer nitrogen saturation adsorption amount, and C is the adsorption capacity constant. The monolayer saturation adsorption amount V_m was determined from the fitted data, and the specific surface area S_g was calculated using:

$$S_g = 4.325 \, V_m \, m^2 \, g^{-1} \tag{2}$$

1.7 Electrochemical Testing

The electrochemical performance of the catalysts was evaluated by immersing the catalysts, grown in situ on nickel foam, into 1.0 M KOH or 0.5 M H_2SO_4 electrolyte solutions. The exposed area was 1×1 cm^2. Electrochemical measurements were performed using a Metrohm Autolab (BV, Utrecht, The Netherlands) electrochemical workstation in a three-electrode setup. The working electrode was the catalyst sample, with a graphite rod as the counter electrode and Ag/AgCl or saturated calomel electrodes as reference electrodes for acidic and alkaline conditions, respectively. Prior to testing, N_2 was purged through the electrolyte to remove dissolved oxygen. The catalysts were activated by CV at a scan rate of 50 mV s^{-1}. Solution resistance was measured, and iR compensation (90%) was applied before LSV measurements. The

recorded potentials versus the reference electrode were converted to the reversible hydrogen electrode (RHE) scale using the Nernst equation:

$E\ (vs.\ RHE) = E0\ (Reference\ ratio) + E\ (Reference\ ratio) + 0.059\ pH$. In acidic conditions, the reference electrode is Ag/AgCl, with $E^0(Ag/AgCl) = 0.197\ V$. In alkaline conditions, the reference electrode is a saturated $Hg/HgCl_2$ electrode, with $E^0(Hg/HgCl_2) = 0.197\ V$. EIS was conducted over a frequency range of 0.1 Hz to 10^{-5} Hz. Stability testing was performed using a constant potential electrolysis approach, where stability was assessed based on the variation in current density under constant overpotential condition

1.8 Density Functional Theory (DFT) Calculations

The first-principles calculations were performed using the Vienna Ab initio Simulation Package (VASP)[S1] with the generalized-gradient-approximation (GGA) in the PBEsol form for the exchange-correlation functional.[S2] The projector augmented wave (PAW) method was employed to describe the core-valence interactions.[S3] A plane-wave energy cutoff of 450 eV was used in all calculations. To accurately capture the magnetic properties, spin polarization was included by setting ISPIN=2. The structural optimization was conducted until the forces on all atoms were reduced to less than 0.02 eV/Å, with an electronic convergence criterion of 1E-5 eV. The van der Waals interactions were taken into account using Grimme's D3 dispersion correction method. The Brillouin zone was sampled using a $1 \times 1 \times 1$ Monkhorst-Pack k-point mesh for the heterostructure.

Considering only the final step of the reaction and taking the desorbed state as the reference point, ΔG is defined as: $\Delta G_{H^*} = \Delta E_{DFT} + \Delta E_{ZPE} - T\Delta_S$, where ΔE_{DFT} is the energy difference of the DFT electrons at each step, ΔE_{ZPE} and $T\Delta_S$ are the zero-point energy correction and entropy change obtained by vibration analysis, respectively. And T = 300 K.

2. Electronic Structure Modifications in Pt-Modified Ni_3S_2/MoS_2 Heterostructures: XPS Analysis

As shown in Figure S1a, the peaks at 853.1 and 866.7 eV correspond to Ni-Ni $2p_{1/2}$ and $2p_{3/2}$, respectively, and the peaks at 855.9 and 873.6 eV correspond to Ni-S $2p_{1/2}$ and $2p_{3/2}$, respectively. Compared with NMS@NF, The Ni-S peak of Pt5-NMS@NF is offset by -0.13 eV, The Ni-S peak of Pt5-NMS@NF shows a -0.13 eV shift compared to NMS@NF, indicating electron cloud density increase on Ni due to electron gain. The fine XPS map of Mo 3d is shown in Figure S1b. Mo 3d can be fitted into two pairs of orbits. The two pairs of peaks at 232.3 and 235.3 eV in NMS@NF are attributed to $3d_{5/2}$ and $3d_{2/3}$ of Mo-O, respectively, which is attributed to high-valence Mo from unavoidable oxidation and incomplete sulfurization. The two peaks at 228.9 eV and 231.1 eV belong to $3d_{5/2}$ and $3d_{3/2}$ of Mo-S, respectively. The Mo-S peaks of Pt5-NMS@NF shift by 0.13 eV to higher binding energy, indicating electron transfer from Mo to Pt, affecting the electronic structure of Ni and Mo atoms in the heterostructure. Mo loses electrons and moves to the high valence state, and the modification of Pt will affect the electronic structure of Ni and Mo atoms in the heterostructure.

The electronic structure changes of the PT-modified heterostructures were further analyzed by combining the XPS fine spectrum of S 2p, as shown in Figure S1c. In NMS@NF, the two peaks at 161.8 and 163.5 eV can be attributed to the $2p_{3/2}$ and $2p_{1/2}$ orbitals of Mo-S, respectively. The two peaks at 162.9 and 164.6 eV can be considered as the $2p_{3/2}$ and $2p_{1/2}$ peaks of Ni-S, while the peaks of Mo-S and Ni-S in Pt5-NMS@NF are offset by 0.33 eV, which indicates that the outermost electrons of S decrease and the electron cloud density decreases. The outer electron orbitals of S produce more vacancies, which is conducive to the adsorption of the S site to the proton source H_2O,[25] which is related to the bonding effect between Pt-S, as shown in Figure S1d. The 71.7 eV and 74.7 eV peaks in the XPS fine spectrum of Pt 4f can be attributed to the $4f_{7/2}$ and $4f_{5/2}$ orbits of Pt, and the other two pairs of peaks at 72.9 and 75.8 eV can be considered to be the $4f_{7/2}$ and $4f_{5/2}$ orbits of the high valence state $PT^{\delta+}$. It can be considered to be generated by the bond formed by the combination of Pt and S.[26] The modification of Pt forms a bond with S, which induces the structural changes of the

electrons Ni, Mo and S on the surface of the heterogeneous structure, and the electrons of Mo and S shift towards the direction of the Ni atom.
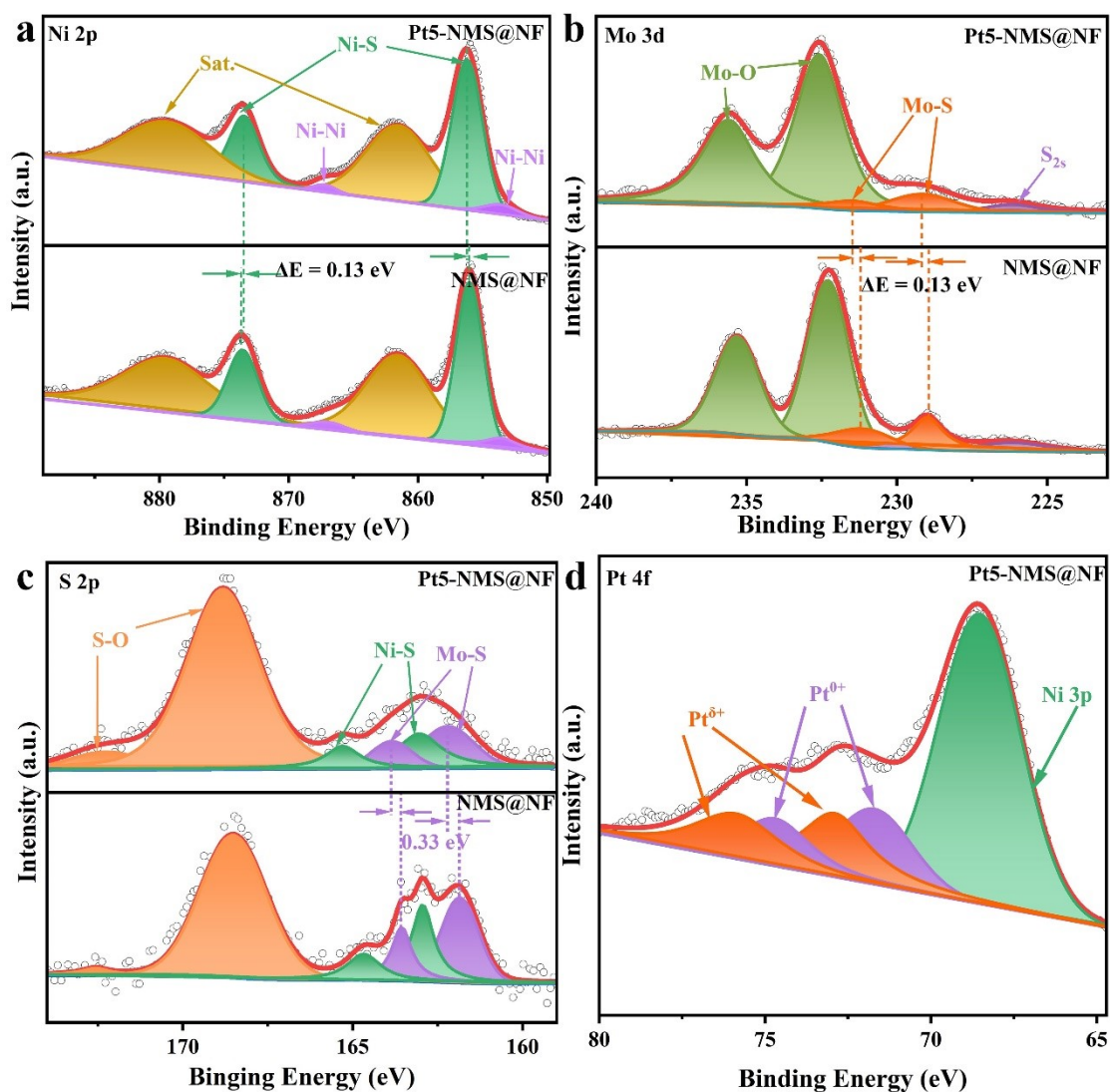

Figure S1. High-resolution XPS spectra of (a) Ni 2p, (b) Mo 3d, (c) S 2p, and (d) Pt 4f for NMS@NF and Pt5-NMS@NF.

3. Analysis of Catalytic Activity and Pt Loading Effects in Pt7-NMS@NF and Pt5-NMS@NF

The LSV curve in Figure 4a shows that although the onset potential of Pt7-NMS@NF is lower than that of Pt5-NMS@NF, the overpotential of Pt7-NMS@NF at 100 mA cm^{-2} is higher. To further explore this point, the LSV curve was normalized (Figure S2), and the results showed that the single-site catalytic activity of Pt7-NMS@NF was higher than that of Pt5-NMS@NF. This may be because after the Pt loading increases, the Pt nanoparticles aggregated on the surface begin to become active

sites, and the excellent catalytic activity of Pt itself makes the catalytic activity of its single site larger. Pt is easy to aggregate, so when Pt is used as a catalyst in large quantities, although the intrinsic activity of the surface is good, the small active surface area also limits its use.[S5] Pt5-NMS@NF has a large active surface area, and the small amount of Pt loading combined with the synergistic effect between Pt-S makes it show more excellent activity in practical applications.
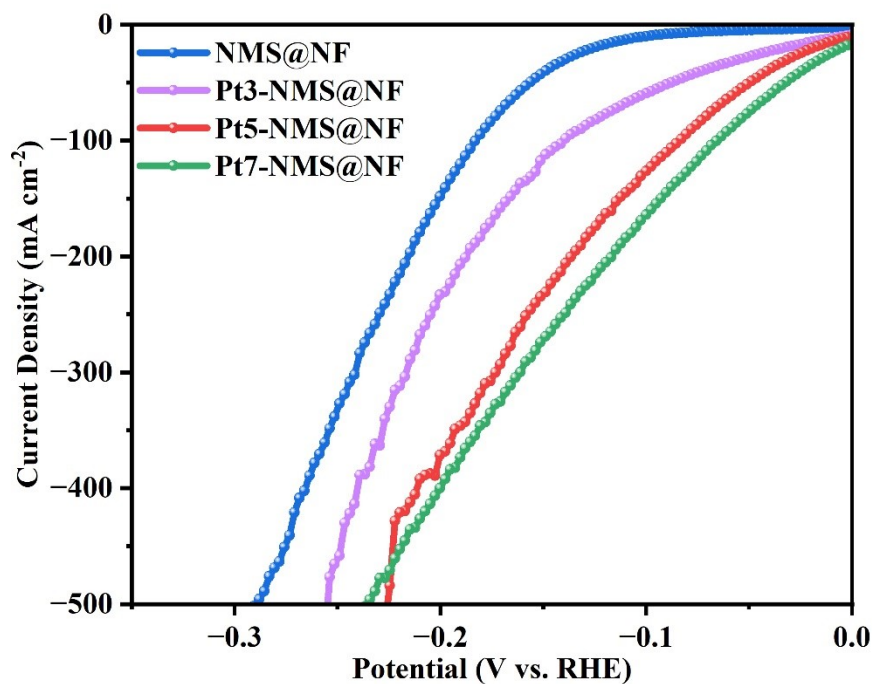

Figure S2. LSV curve after ECSA normalization.
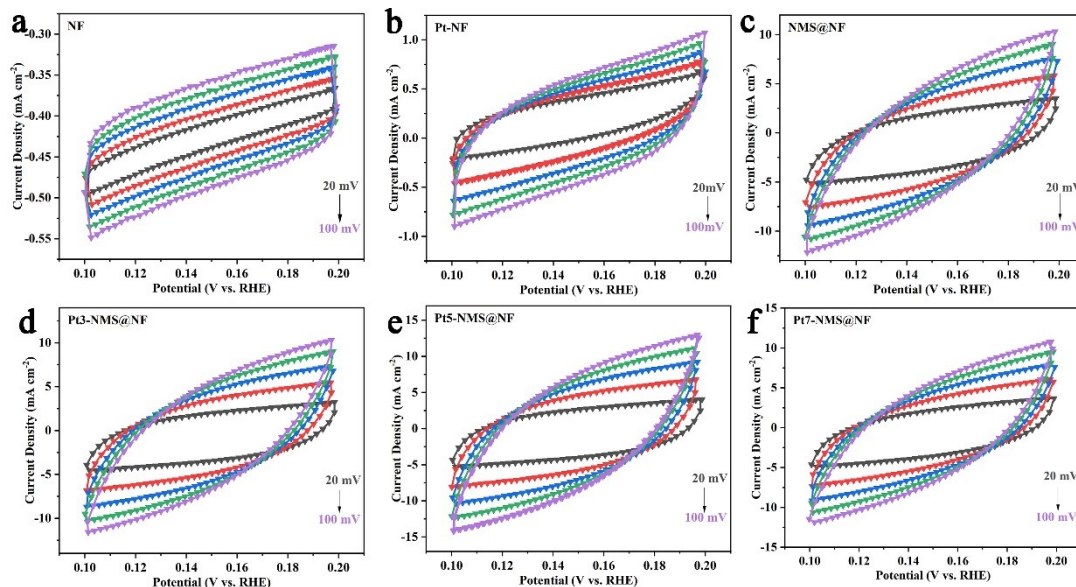
Figure S3. CV curves of (a) NF, (b) Pt-NF, (c) NMS@NF, (d) Pt3-NMS@NF, (e) Pt5-NMS@NF and (f) Pt7-NMS@NF catalysts at different scanning rates under alkaline conditions.
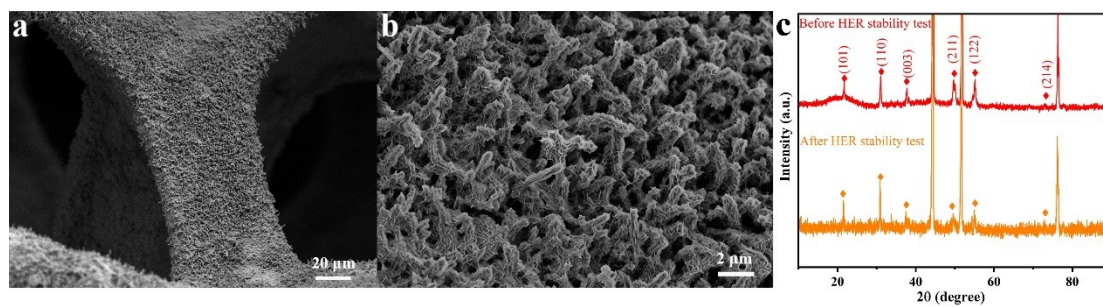
Figure S4. SEM image and XRD pattern of HER stability test under alkaline conditions.

$$H_2O \rightarrow H^* + OH^-$$

$$H^* + H_2O \rightarrow H_2 + OH^-$$

S   Mo   Ni   Pt   O   H
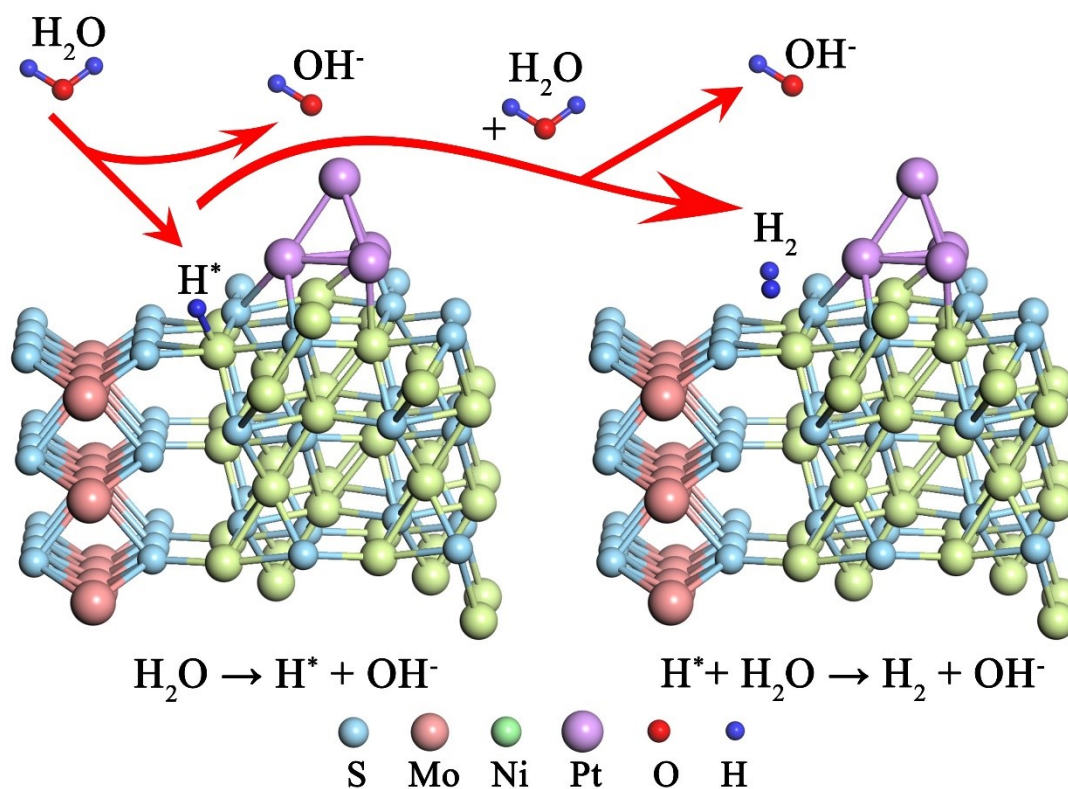
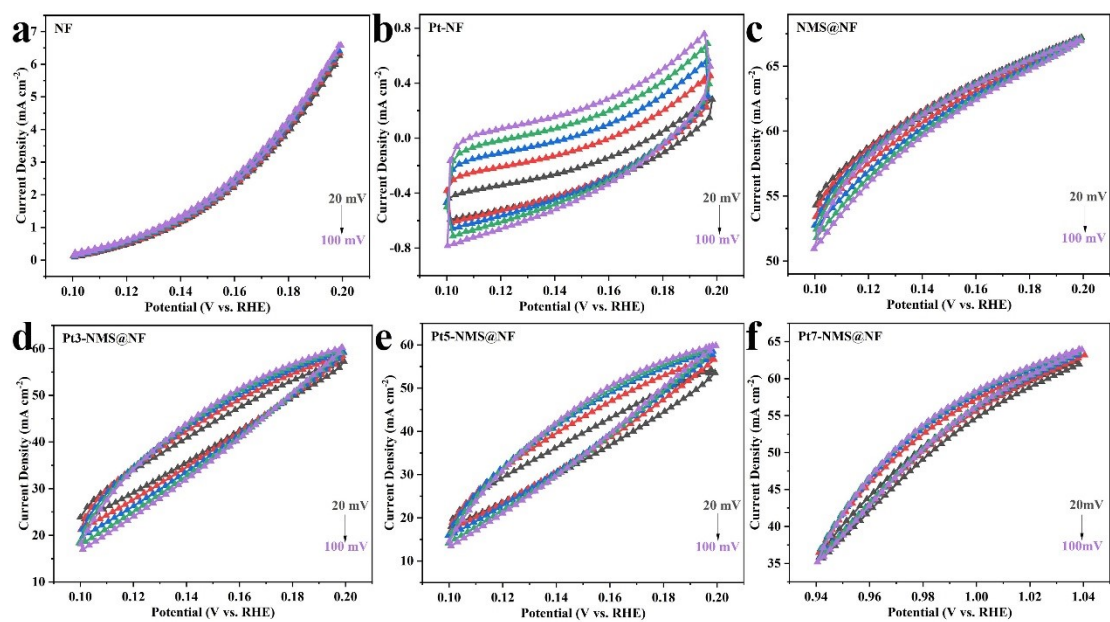Figure S5. Schematic diagram of the reaction mechanism for the HER of the catalyst Pt5-

NMS@NF.

Figure S6. CV curve at different scan rates of (a) NF, (b) Pt-NF, (c) NMS@NF, (d) Pt3-NMS@NF, (e) Pt5-NMS@NF and (f) Pt7-NMS@NF catalysts under acidic conditions.
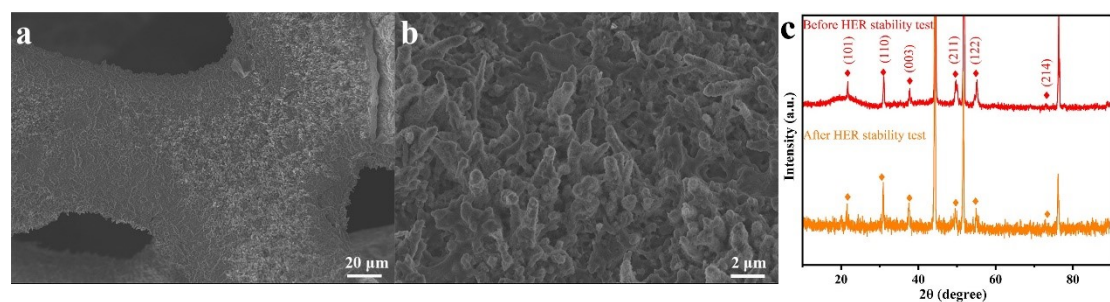

Figure S7. SEM image and XRD pattern of HER stability test under acidic conditions.
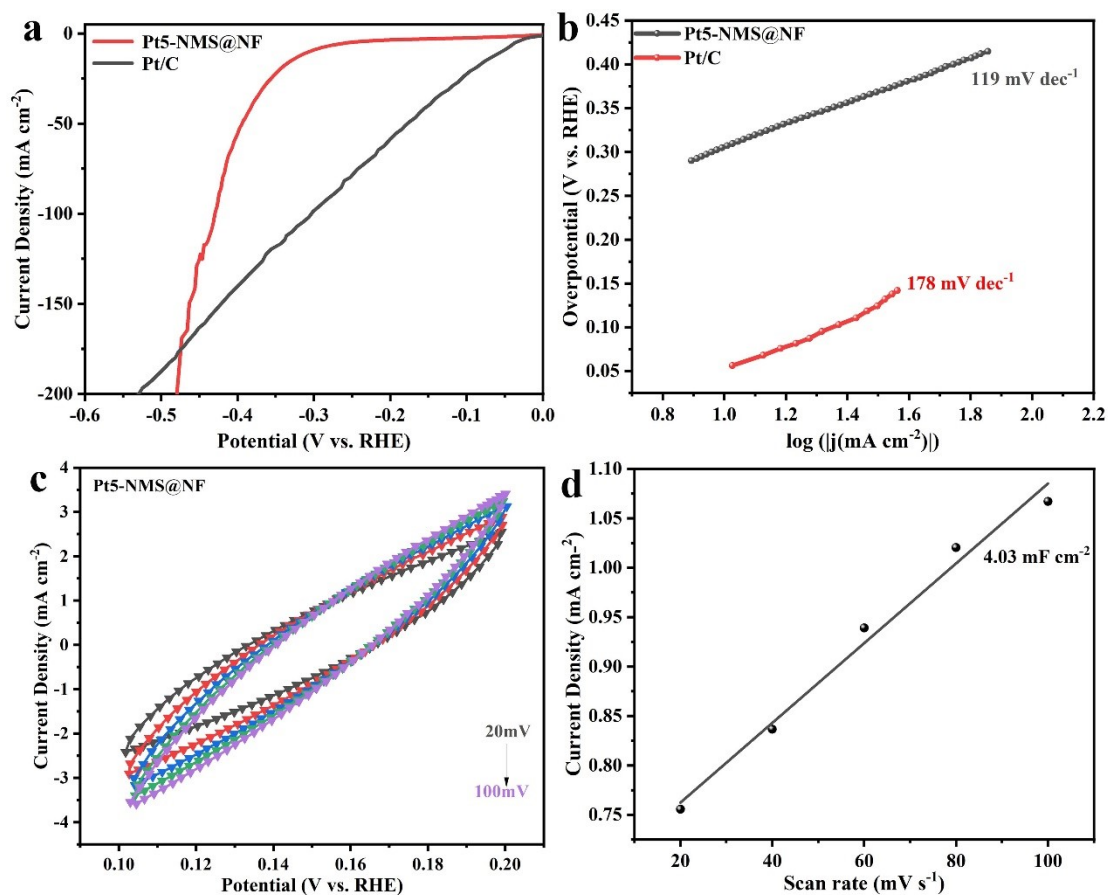
Figure S8. (a) LSV curve, (b) Tafel slope, (c) CV curve, and (d) ECSA of the catalyst Pt5-NMS@NF at neutral conditions.
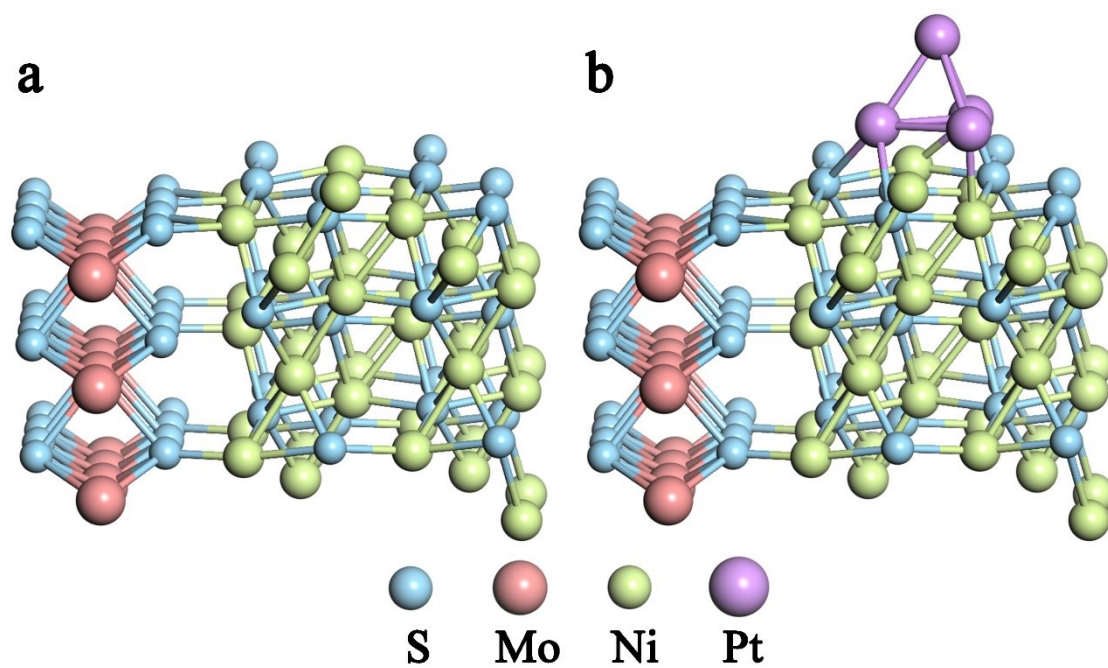

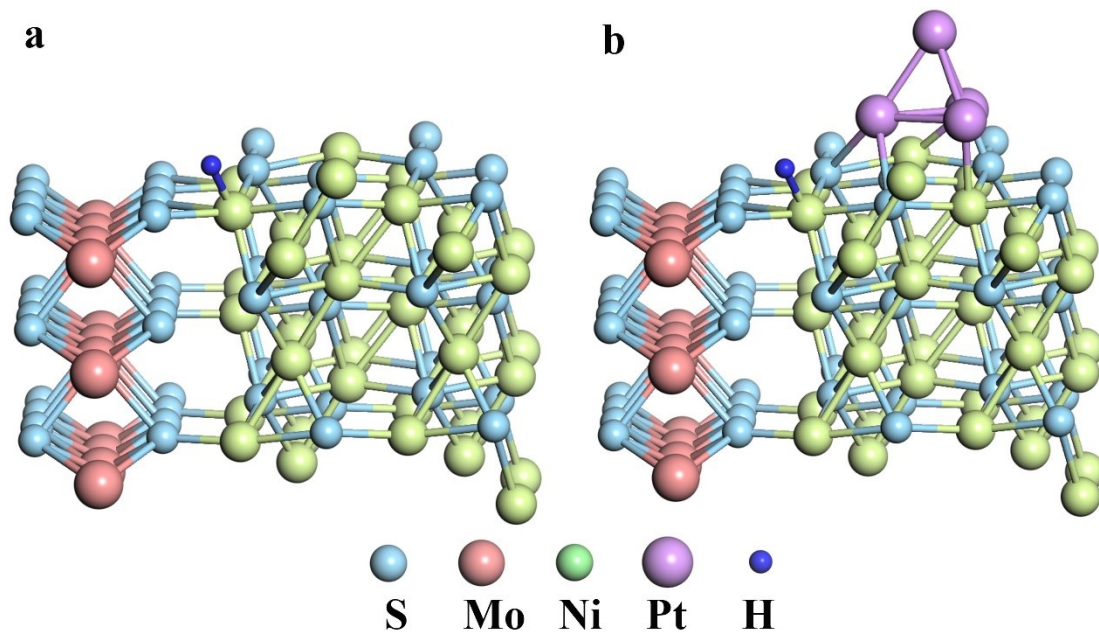Figure S9. (a) NMS@NF, (b) Pt-NMS@NF heterojunction structure.

Figure S10. The hydrogen adsorption structure of (a, b) NMS@NF and Pt-NMS@NF.

Table S1. Comparison of the HER performances in alkaline solution for some transition metal-based HER catalysts reported recently.

Catalyst	Electrolyte	η_{100}(mV)	Tafel slope(mV dec-1)	Ref.
MoS$_2$–Ni$_3$S$_2$ HNRs/NF	1.0 M KOH	191	61	[S6]
P-MoS$_2$–Ni$_3$S$_2$/NF	1.0 M KOH	263	40.95	[S8]
P$_{40}$-MoS$_2$/Ni$_3$S$_2$-5	1.0 M KOH	142	107.2	[43]
CoFe-P/NF-1	1.0 M KOH	180	84	[S9]
Co$_2$P-200 HMT/NF	1.0 M KOH	159	68.6	[S10]
Co-NiS$_2$/MoS$_2$	1.0 M KOH	166	63.3	[S11]
Graphene/MoS$_2$/FeCoNiP	1.0 M KOH	127	25.2	[S12]
MoS$_2$/Ni$_3$S$_2$/NiFe-LDH/NF	1.0 M KOH	261	141	[S13]
SnS$_2$/MoS$_2$/Ni$_3$S$_2$/NF	1.0 M KOH	232	107.71	[S14]
Pt5-NMS@NF	1.0 M KOH	64	68	This work

Table S2. Comparison of the OER performances in alkaline solution for some transition metal-based OER catalysts reported recently.

Catalyst	Electrolyte	η_{100}(mV)	Tafel slope(mV dec^{-1})	Ref.
MoS$_2$–Ni$_3$S$_2$ HNRs/NF	1.0 M KOH	341	57	[S6]
NiFe-LDH/MoS$_2$-Ni$_3$S$_2$/NF	1.0 M KOH	347	108	[S7]
P-MoS$_2$–Ni$_3$S$_2$/NF	1.0 M KOH	449	34.67	[S8]
P40-MoS$_2$/Ni$_3$S$_2$-5	1.0 M KOH	278	116.7	[43]
Co-NiS$_2$/MoS$_2$	1.0 M KOH	384	132.2	[S11]
MoO$_3$/Ni-NiO	1.0 M KOH	347	60	[S14]
Pt5-NMS@NF	1.0 M KOH	275	35	This work

Table S3. Partial composition of elements in the Pt5-NMS@NF sample.

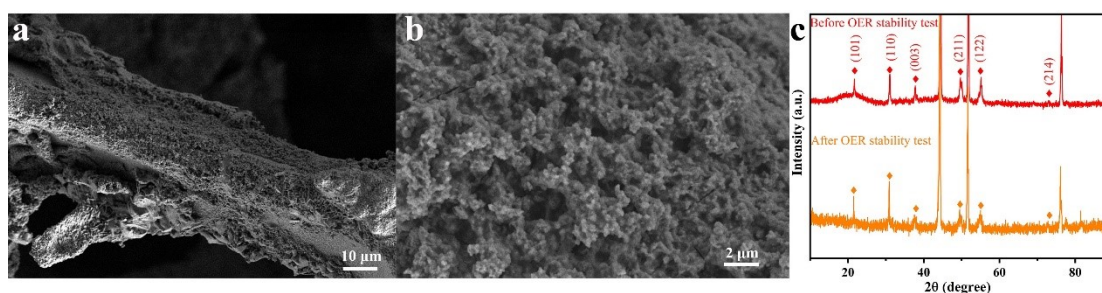| Element	Peak Position(BE)	FWHM(eV)	Area(CPS.eV)	Atomic(%)
O 1s	531.13	2.23	126281.62	45.54
C 1s	284.80	2.02	32274.79	28.15
Ni 2p	855.79	3.13	290345.56	19.74
S 2p	168.49	2.52	8067.53	3.48
Pt 4f	68.22	3.44	35851.27	1.65
Mo 3d	232.31	2.15	18779.34	1.44

Figure S11. SEM image and XRD pattern of OER stability test under alkaline condition.
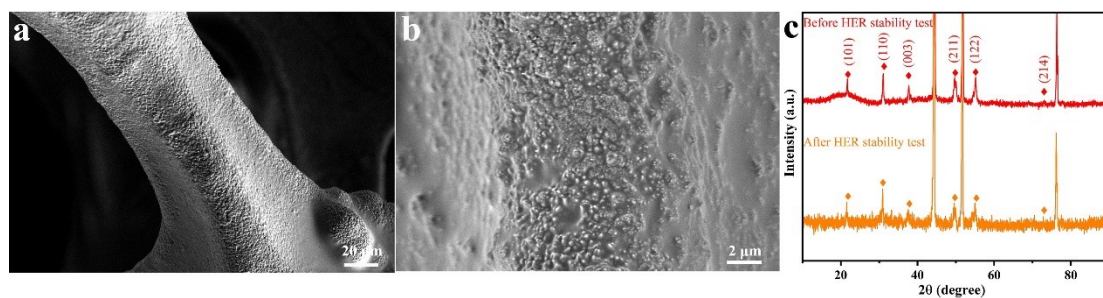
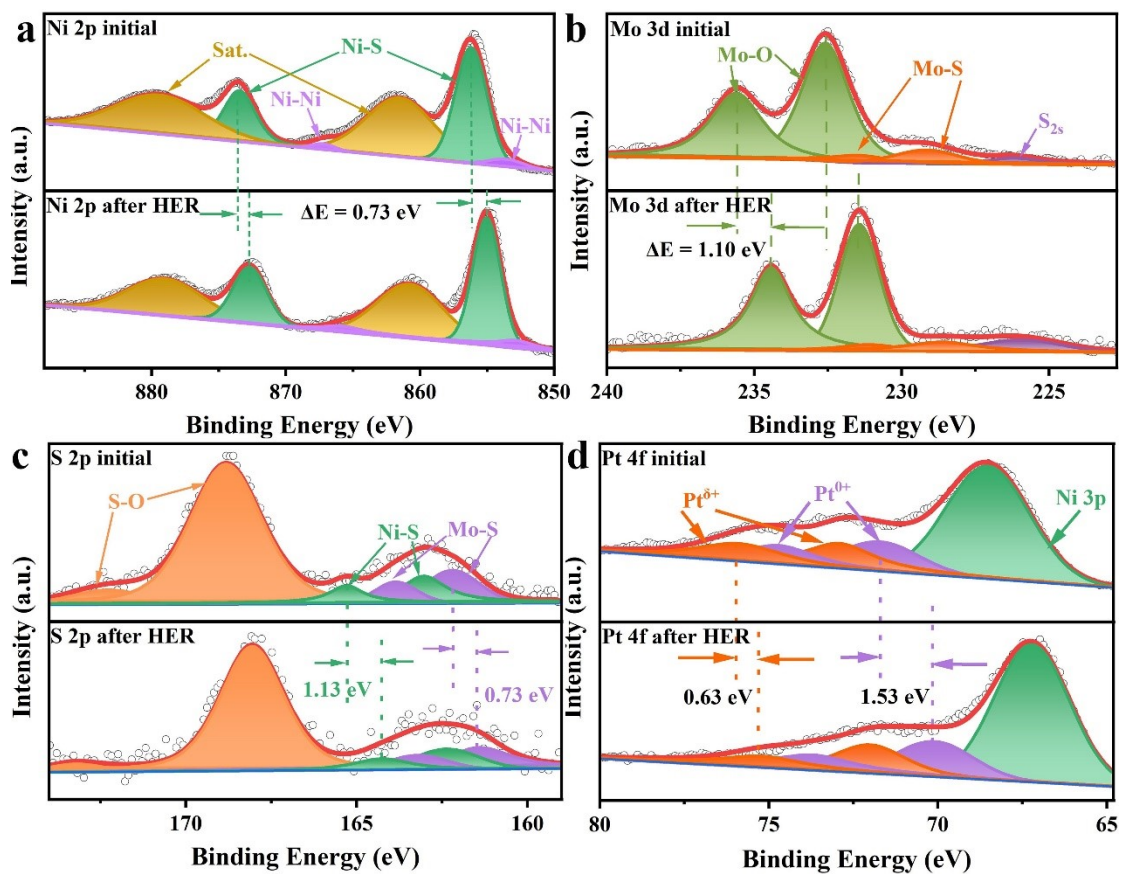Figure S12. SEM image and XRD pattern of HER test under neutral conditions.

Figure S13. XPS of Pt5-NMS@NF before and after HER stability test under alkaline conditions (a)
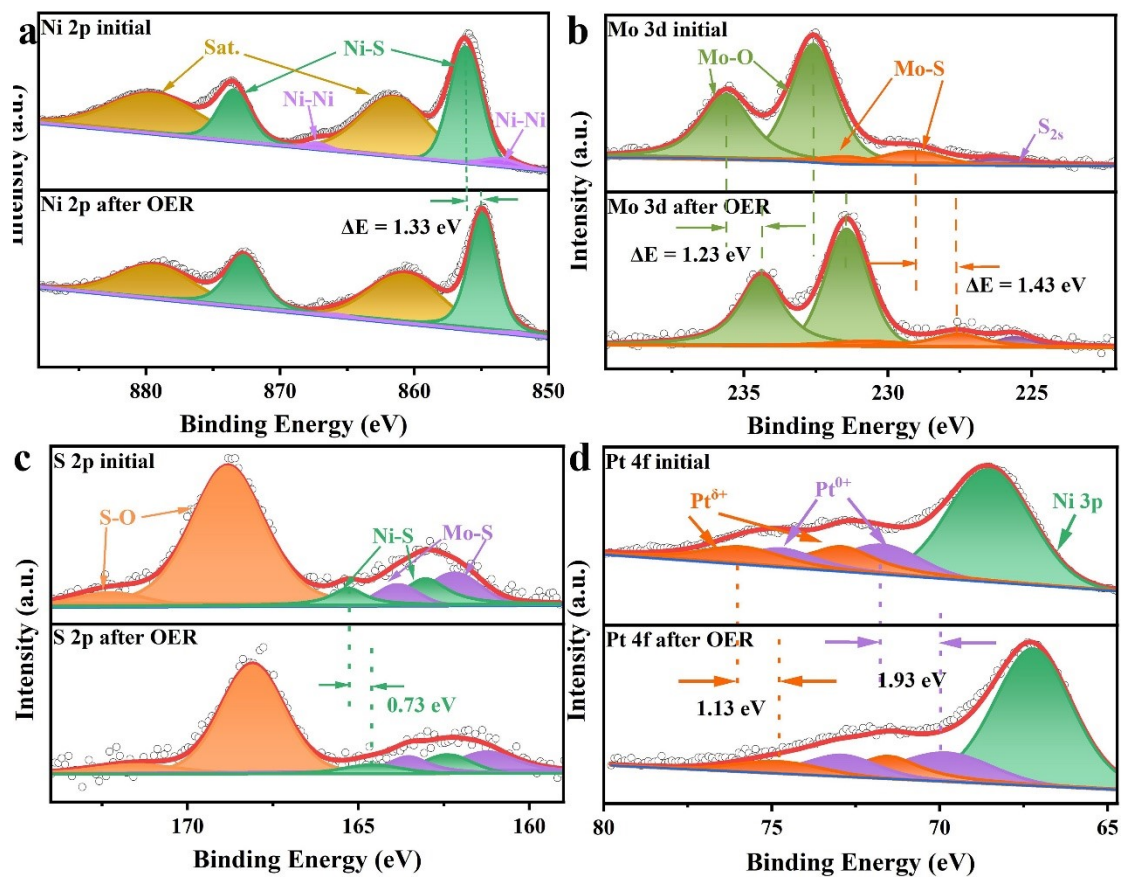
Ni 2p, (b) Mo 3d, (c) S 2p and (d) Pt 4f.

Figure S14. XPS of Pt5-NMS@NF before and after OER stability test under alkaline conditions (a)

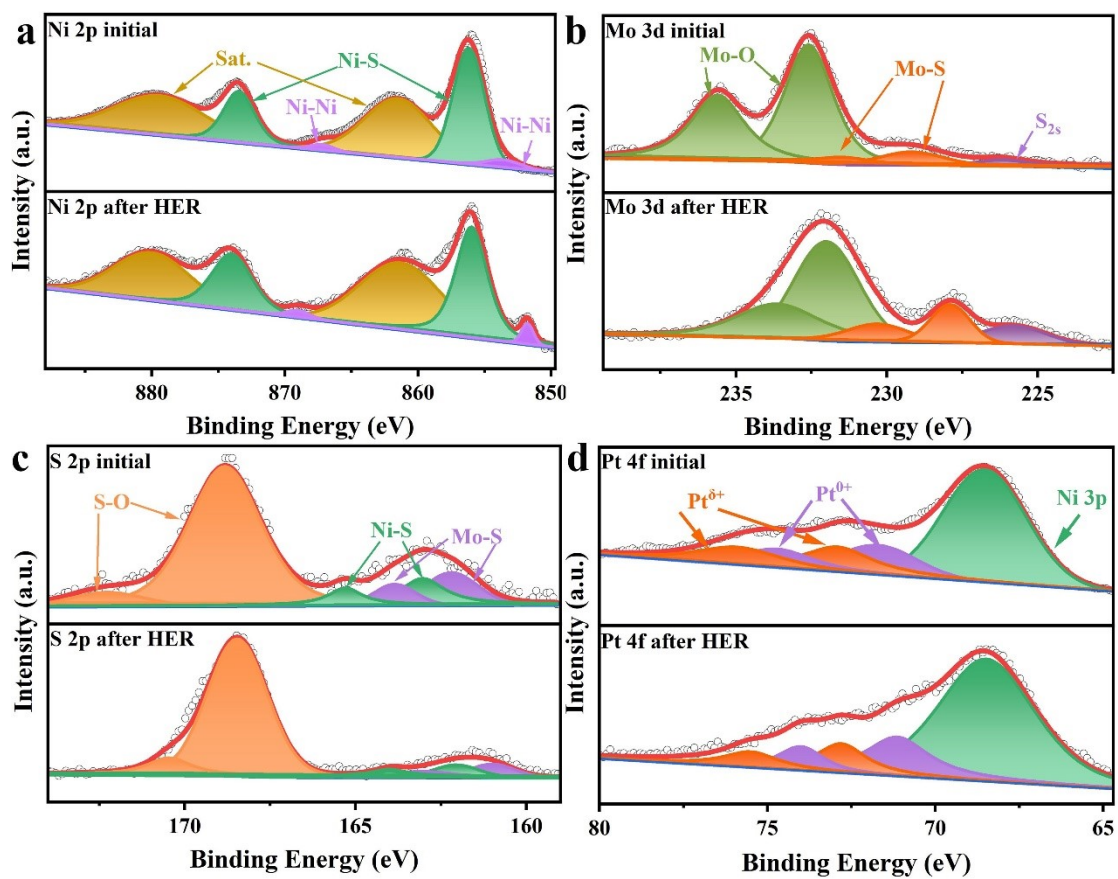Ni 2p, (b) Mo 3d, (c) S 2p and (d) Pt 4f.

Figure S15. XPS of Pt5-NMS@NF before and after HER stability test under acidic conditions (a) Ni 2p, (b) Mo 3d, (c) S 2p and (d) Pt 4f.
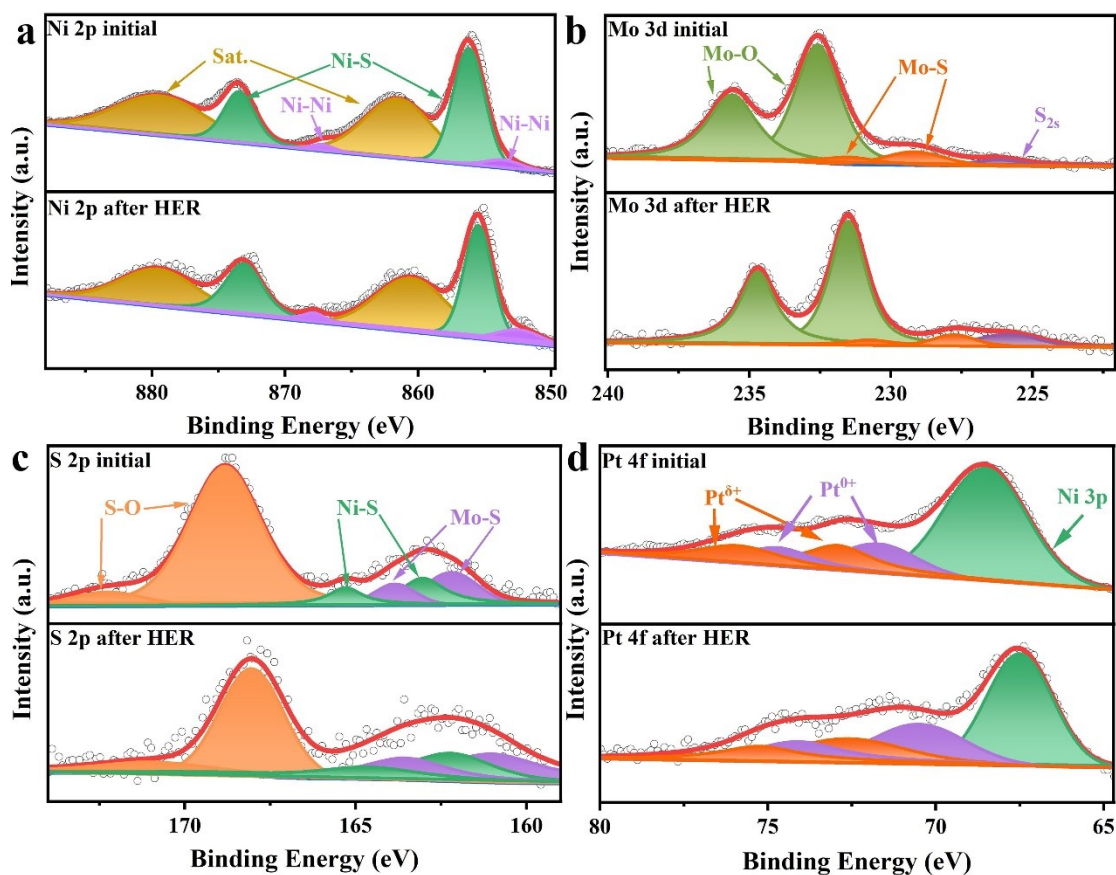
Figure S16. XPS of Pt5-NMS@NF before and after HER stability test under neutral conditions (a) Ni 2p, (b) Mo 3d, (c) S 2p and (d) Pt 4f.

Reference

[S1] J.P. Perdew, K. Burke and M. Ernzerhof, *Phys. Rev. Lett.*, 1996, **77**, 3865.

[S2] G. Kresse, J. Furthmüller, *Phys. Rev. B*, 1996, **54**, 11169.

[S3] P.E. Blöchl, *Phys. Rev. B*, 1994, **50**, 17953.

[S4] A. Tkatchenko, M. Scheffler, *Phys. Rev. Lett.*, 2009, **102**, 073005.

[S5] Y. Zhu, Z. Qu and G. Zhang, *Electrochim. Acta*, 2024, **475**, 143590.

[S6] S. Wang, X. Ning and Y. Cao, *Inorg. Chem.*, 2023, **62**, 6428-6438.

[S7] Y. Yang, K. Zhang and H. Liu, *Acs Catal.*, 2017, **7**, 2357-2366.

[S8] Y. Miao, S. Yuan and H. Ren, *ACS Appl. Energy Mater.*, 2023, **6**, 5856-5867.

[S9] X. Wang, C. Wang and F. Lai, *ACS Appl. Nano Mater.*, 2021, **4**, 12083-12090.

[S10]　T. Wang, C. Wang and Y. Ni, *Chem. Commun.*, 2022, **58**, 6352-6355.

[S11]　N. Cao, S. Chen and Y. Di, *Electrochim. Acta*, 2022, **425**, 140674.

[S12]　X. Ji, Y. Lin and J. Zeng, *Nat. Commun.*, 2021, **12**, 1380.

[S13]   M. He, S. Hu and C. Feng, *Int. J. Hydrogen Energ.*, 2020, **45**, 23-35.

[S14]   J. Li, Y. Lv and X. Wu, *Colloid. Surface. A.*, 2023, **670**, 131634.